Research Article | Vol. 32, No. 20 / 23 Sep 2024 / Optics Express 35755

Optics EXPRESS

Analytical form of the refocused images from correlation plenoptic imaging

GIANLORENZO MASSARO[1,2,*]

[1]Dipartimento di Fisica, Universitá di Bari, I- 70125 Bari, Italy
[2]INFN - Sezione di Bari, I- 70125 Bari, Italy
[*]gianlorenzo.massaro@uniba.it

Abstract: Correlation plenoptic imaging (CPI) is emerging as a promising approach to light-field imaging (LFI), a technique for concurrently measuring light intensity distribution and propagation direction of light rays from a 3D scene. LFI thus enables single-shot 3D imaging, offering rapid volumetric reconstruction. The optical performance of traditional LFI, however, is limited by a micro-lens array, causing a decline in resolution as 3D capabilities improve. CPI overcomes these limitation by measuring photon number correlations on two photodetectors with spatial resolution, in a lenslet-free design, so that the correlation function can be decoded in post-processing to reconstruct high-resolution images. In this paper, we derive the analytical expression of CPI images reconstructed through refocusing, addressing the previously unknown mathematical relationship between object shape and its final image. We show that refocused images are not limited by numerical aperture-induced blurring, as in conventional imaging. Rather, the image features of CPI can be explained through an analogy with imaging systems illuminated by spatially coherent light.

1. Introduction

The study of light correlations has long been of interest due to their potential to enhance traditional measurement techniques [1–8]. Investigations into correlations in both classical and quantum contexts have yielded significant advancements, particularly in imaging technologies [9–24]. In the quantum domain, the unique properties of entanglement have been exploited to exceed the sensitivity limits of traditional imaging methods [25]. This has led to breakthroughs such as sub-shot-noise microscopy [26,27], enabling unprecedented precision in imaging amplitude and phase samples [28]. Interestingly, similar correlation properties can also be observed in classical systems; this convergence of quantum and classical approaches demonstrates that many protocols initially designed for quantum applications can be effectively adapted to classical contexts [9,29–32]. As a result, the study of correlations continues to bridge the gap between quantum and classical imaging, offering versatile solutions that transcend traditional boundaries. Correlation plenoptic imaging (CPI) [33–39] is emerging as a promising correlation-based approach to light-field imaging (LFI). LFI is a technique that allows for the concurrent measurement of both light intensity distribution and the propagation direction of light rays from a three-dimensional scene of interest [40]. The extensive amount of information collected by a light-field device enables single-shot 3D sampling, a task that would require multiple acquisitions across various planes with a standard camera [41,42]. This scanning-free characteristic makes light-field imaging one of the fastest methods for 3D reconstruction, with applications spanning diverse fields such as photography [43–45], microscopy [46] and real-time imaging of neuronal activity [47]. Typically, light-field imaging employs an array of micro-lenses positioned between the sensor and the imaging device (*e.g.*, the camera lens). However, the presence of the array significantly limits image resolution, preventing it from reaching the diffraction limit and causing a rapid decline in resolution as 3D reconstruction capabilities improve [48,49]. CPI addresses the main limitation of conventional LFI by decoupling the measurement of light-field information

#533669 https://doi.org/10.1364/OE.533669
Journal © 2024 Received 21 Jun 2024; revised 30 Jul 2024; accepted 31 Jul 2024; published 19 Sep 2024

Optics EXPRESS

onto two photodetectors with spatial resolution [33], utilizing a lenslet-free optical design. Three-dimensional information about the sample is encoded in the four-dimensional correlation function, obtained by correlating the instantaneous light intensity impinging on the sensors and performing statistical averaging. This correlation function can then be decoded entirely in post-processing, to reconstruct high-resolution images of the object without the loss of resolution typical of conventional LFI.

In this paper, we shall obtain the analytical expression of the CPI images reconstructed through *refocusing* [50]. The mathematical relationship between the object shape and its final image, in fact, was not known. For these reason, the optical performance of the technique has always been evaluated based on phenomenological evidence, namely, by quantifying image degradation as a function of the axial position of the sample. However, the typical source of degradation of CPI images is not blurring, as is the case with conventional imaging, but *fringing* effects [34,38], which alter the object features and are considered as artifacts of the technique. Finding the mathematical expression of the final image, finally allows us to associate the image quality of CPI to a well-defined physical origin, demonstrating a perfect analogy with many of the features characterizing imaging systems illuminated by spatially coherent light.

2. Materials and methods

2.1. Imaging properties of CPI and refocusing

In CPI, light-field information about the sample is gathered by measuring intensity, or photon number, correlations on two spatially resolving detectors.

$$\Gamma(\boldsymbol{r}_a, \boldsymbol{r}_b) = \langle I_A(\boldsymbol{r}_a) I_B(\boldsymbol{r}_b) \rangle - \kappa \langle I_A(\boldsymbol{r}_a) \rangle \langle I_B(\boldsymbol{r}_b) \rangle , \tag{1}$$

where $I_{A,B}$ is the instantaneous intensity on the detectors [51], and $\boldsymbol{r}_{a,b} = (x_{a,b}, y_{a,b})$ are the two-dimensional coordinates on the two detectors photosensitive surface; $\langle I \rangle$ represents the ensemble average of the stochastic quantity I. The value of the constant $\kappa = 0, 1$ varies according to the selected illumination source of choice: for entangled-photon illumination $\kappa = 0$ [52–54], whereas, with thermal light intensity *fluctuations* ($\kappa = 1$) are correlated [34,36,54,55]. Without loss of generality for the scope of this work, we shall assume henceforth that $\kappa = 1$.

CPI can be implemented in many variations, each optimized for a specific goal according to the application of interest and features of the sample. However, the correlation function is always mathematically described through a second-order response function Φ'

$$\Gamma(\boldsymbol{r}_a, \boldsymbol{r}_b) = \left| \int A(\boldsymbol{r}_s) \int \left[A^*(\boldsymbol{r}'_s) \right]^m \Phi'(\boldsymbol{r}_s, \boldsymbol{r}'_s, \boldsymbol{r}_a, \boldsymbol{r}_b) \, d\boldsymbol{r}'_s \, d\boldsymbol{r}_s \right|^2 , \tag{2}$$

establishing the relationship between the electric field at the detectors coordinates and the field on the sample coordinates (see Ref. [51] for a complete formal context). In the equation, $A(\boldsymbol{r}_s)$ represents the *complex* electric field transmittance of a 2D sample, where m can either be 0, if only one of the two detectors collects light from the object, or 1 if light from the sample illuminates both sensors [51]. The optical response of CPI is thus strongly non-linear with respect to the input function A, both because A is involved twice in the second-order response function, and because of the square module [56]. In many cases of interest Eq. (2) can be written as [57]

$$\Gamma(\boldsymbol{r}_a, \boldsymbol{r}_b) = \left| \int A(\boldsymbol{r}_s) \left[A^*(\boldsymbol{r}_s) \right]^m \Phi(\boldsymbol{r}_s, \boldsymbol{r}_a, \boldsymbol{r}_b) \, d\boldsymbol{r}_s \right|^2 . \tag{3}$$

For definiteness, we shall limit our discussion to phase-insensitive architectures ($m = 1$), even though the results we shall present can be effortlessly extended to the case $m = 0$. None of our assumption throughout the work, however, limit the validity of our analysis to either the

Optics EXPRESS

macroscopic light intensity regime [34] or to coincidences at the single photon level [35], so that the results obtained in this work apply equally well to both scenarios.

In order to obtain a sharp, axially localized [57], and low-noise image [58,59], the Γ function must be *refocused*; the refocusing procedure is thoroughly described in Refs. [50,51]. In few words, refocusing consists of reconstructing a specific object coordinate $\boldsymbol{r}$ by integrating over all the optical paths converging from the two detectors to the sample coordinate $\boldsymbol{r}$ of interest [50,51,53]. The reconstruction at coordinate $\boldsymbol{r} = (x, y)$ is thus obtained by means of the double line integral

$$\Sigma_z(\boldsymbol{r}) = \int_{\gamma_x(x,z)} \int_{\gamma_y(y,z)} \Gamma \, d\ell_x d\ell_y, \tag{4}$$

where the integration paths $\gamma_x(x, z)$ in the (x_a, x_b) plane, and $\gamma_y(y, z)$ in the (y_a, y_b) have equations

$$\gamma_x(x, z) : \alpha(z)\, x_a + \beta(z)\, x_b = x \tag{5}$$

$$\gamma_y(y, z) : \alpha(z)\, y_a + \beta(z)\, y_b = y. \tag{6}$$

As inferred by the dependence on z of the two coefficients α and β, the axial coordinate z of the reconstructed plane is determined by the slope of the integration path, controlled, in turn, by α and β. Depending on the optical design of the experiment, the functional dependence of the coefficients on z is governed by the optical distances and experimental parameters into play.

2.2. Analytical expression of the reconstructed image

The exact mathematical expression that relates the object transmission function $A(\boldsymbol{r}_s)$, placed at axial coordinate z, and its reconstructed image $\Sigma_z(\boldsymbol{r})$ is not as as straightforward as in typical imaging devices. It is customary, in imaging, to describe the optical behavior of the imaging systems in terms of its point-spread function (PSF), so that the image of an sample is obtained by convolution of the object intensity profile with the PSF [60]. Such is the case, for instance, of conventional LFI, in which the width of the PSF (or resolution) is determined by the combination of the NA of the optical design and the size of the lenslets [61]. Conversely, due to both the non-linearity of Eq. (2) and the added complexity originating from the refocusing procedure, the mathematical relationship between the input shape and the output image in CPI is more complicated and cannot be described through a PSF.

We shall now give an overview of the steps required to obtain an analytical form of the reconstructed image. As detailed in Ref. [50], the refocusing procedure entails a reparametrization of the correlation function, so that the two line integrals in Eq. (4) can be evaluated, either numerically or analytically, as Riemann integrals

$$\Sigma_z(\boldsymbol{r}) = \int_{\gamma_x(x,z)} \int_{\gamma_y(y,z)} \Gamma \, d\ell_x d\ell_y = \int \int \Gamma_{\text{trans}} \left(x, y, t_x, t_y\right) \, dt_x \, dt_y, \tag{7}$$

where the transformed correlation function Γ_{trans}, also known as the refocused correlation function, is a reparametrization of the original Γ:

$$\Gamma_{\text{trans}} \left(x, y, t_x, t_y\right) = \Gamma(x_a(x, t_x),\, y_a(y, t_y),\, x_b(x, t_x),\, y_b(y, t_y)). \tag{8}$$

Refocusing is thus defined by the *linear* refocusing transformation

$$\begin{bmatrix} x_a(x, t_x) \\ x_b(x, t_x) \end{bmatrix} = R_z \begin{bmatrix} x \\ t_x \end{bmatrix}, \tag{9}$$

where R_z is the 2×2 *refocusing matrix* in the (x, t_x) plane. The analogous relationship holds for defining the dependence on the remaining two dimensions $y_a(y, t_y)$ and $y_b(y, t_y)$. The refocusing

Optics EXPRESS

matrix R_z is linked to the refocusing integration path of Eqs. (5) and (6) through its inverse matrix

$$R_z^{-1} = \begin{bmatrix} \alpha(z) & \beta(z) \\ \xi & \zeta \end{bmatrix}, \tag{10}$$

where the first row of the matrix is determined by the coefficients of the integration path, while the second row is completely arbitrary, provided $\det R_z^{-1} \neq 0$ (R_z^{-1} must be invertible to obtain the refocusing matrix). The mathematical expression of $\Sigma_z(\boldsymbol{r}_s)$ is thus obtained by arbitrarily choosing the second row of the matrix R_z^{-1} and inverting it, to obtain the functional dependence of Eq. (9); the expressions in Eq. (9) must then be plugged into the function Φ' of Eq. (2) to obtain the refocused correlation function Γ_{trans}; lastly, the double integral on (t_x, t_y) must be performed. Although the outlined steps lead to a perfectly determined mathematical formula, its analytical expression is cumbersome and difficult to interpret, with the added downside of not being universal for any CPI architecture, because both the function Φ' and the refocusing matrix R_z depend on the optical design.

3. Results

3.1. Refocusing in the infinite-NA approximation

It is well known that the quality of refocused images is almost unaffected by the NA of the optical design [34,35,55,57]. In fact, apart from the plane (or planes [54]) in focus, available at Rayleigh-limited resolution λ/NA, the *quality* of the refocused images can be accurately predicted in the limit of infinitely large optical components [57]. The simplified scenario of infinite NA is surely worth investigating, since, as we shall see shortly, it allows one to develop a clear picture for interpreting the features of the refocused images. To this end, let us consider that a CPI system described by Eq. (3) with $m = 1$ has [51,53]

$$\Phi(\boldsymbol{r}_s, \boldsymbol{r}_a, \boldsymbol{r}_b) = g_a(\boldsymbol{r}_s, \boldsymbol{r}_a)\, g_b^*(\boldsymbol{r}_s, \boldsymbol{r}_b), \tag{11}$$

where $g_{a,b}$ are the Green's functions propagating the electric field from the object plane at coordinate $\boldsymbol{r}_s$ to the detector plane at coordinate $\boldsymbol{r}_{a,b}$, respectively. As schematically outlined in Fig. 1, any CPI architecture where the object shows negligible coherence area on its surface [58,59], can be brought back to a simple conceptual scheme: light emitted from the object propagates through free space until it reaches the planes that are optically conjugated to each detector, placed at a distance z_a and z_b, respectively; from the focused planes, the electric field is then relayed, through the imaging systems A and B, onto the two detectors, with magnifications M_a and M_b respectively. With this picture in mind, the Green's function in Eq. (11) can always be written as

$$g_{a,b}(\boldsymbol{r}_s, \boldsymbol{r}_{a,b}) = \int \exp\left[i \frac{\pi}{\lambda \left(z - z_{a,b}\right)} (\boldsymbol{r}_s - \boldsymbol{r}_0)^2 \right] \mathcal{P}_{a,b}\left(\boldsymbol{r}_0, \frac{\boldsymbol{r}_{a,b}}{M_{a,b}}\right) d\boldsymbol{r}_0, \tag{12}$$

where the first integrand function represents free-space propagation by an optical distance $z - z_{a,b}$ (which can be negative for backwards propagation) [62] and $\mathcal{P}_{a,b}$ represents the PSF of the focused imaging systems A and B, respectively. In the infinite-NA approximation that we shall adopt, the planes in focus are thus relayed on the two detectors with perfect accuracy ($\mathcal{P}_{a,b}\left(\boldsymbol{r}_o, \boldsymbol{r}_{a,b}/M_{a,b}\right) \to \delta^{(2)}\left(\boldsymbol{r}_o - \boldsymbol{r}_{a,b}/M_{a,b}\right)$), so that Eq. (11) reduces to a pure-phase term

$$\Phi_\infty(\boldsymbol{r}_s, \boldsymbol{r}_a, \boldsymbol{r}_b) = \lim_{\text{NA}\to\infty} \Phi(\boldsymbol{r}_s, \boldsymbol{r}_a, \boldsymbol{r}_b) = \exp\left[i \frac{\pi}{\lambda} \left(\frac{(\boldsymbol{r}_s - \boldsymbol{r}_a/M_a)^2}{z - z_a} - \frac{(\boldsymbol{r}_s - \boldsymbol{r}_b/M_b)^2}{z - z_b} \right) \right]. \tag{13}$$

This expression, valid for any CPI architecture, can also be used as a quick alternative way to find the refocusing coefficients α and β in all generality. Through a stationary phase

Optics EXPRESS

approximation [53], in fact, one finds that the refocusing integration paths $\boldsymbol{r}(\boldsymbol{r}_a, \boldsymbol{r}_b)$, solving

$$\left.\frac{\partial \arg \Phi}{\partial \boldsymbol{r}_s}\right|_{\boldsymbol{r}_s=\boldsymbol{r}(\boldsymbol{r}_a,\boldsymbol{r}_b)} = 0, \tag{14}$$

have equations

$$\gamma_x(x,z) : x = \frac{z-z_b}{z_a-z_b}\frac{x_a}{M_a} - \frac{z-z_a}{z_a-z_b}\frac{x_b}{M_b} = \alpha(x)\, x_a + \beta(z)\, x_b, \tag{15}$$

for the x component, and analogous equation for the y components, exactly as expected from Eqs. (5) and (6). The coefficients α and β can thus be used to build the refocusing matrix R_z and the refocused correlation function. In the infinite-NA approximation, one finds an interesting result: once the correlation is transformed, its dependence on the two integration parameters is lost

$$\frac{\partial \Gamma^{(\infty)}_{\text{trans}}}{\partial t_{x,y}} = 0, \tag{16}$$

so that

$$\Sigma^{(\infty)}_z(\boldsymbol{r}) \propto \Gamma^{(\infty)}_{\text{trans}}(\boldsymbol{r}) = \left| \int |A(\boldsymbol{r}_s)|^2 \exp\left[i \frac{\pi}{\lambda\, d(z)} (\boldsymbol{r}_s - \boldsymbol{r})^2 \right] d\boldsymbol{r}_s \right|^2, \tag{17}$$

with

$$d(z) = \left(\frac{1}{z-z_a} - \frac{1}{z-z_b} \right)^{-1}. \tag{18}$$

Equation (17) is easily recognized as the *coherent* diffraction pattern [60,62] of the *intensity* profile of the object, as observed after Fresnel diffraction by an *equivalent distance* $d(z)$. The second integrand function is, in fact, the free-space propagator, already used in Eq. (12) to propagate the electric field towards the planes in focus. Interestingly, the equivalent propagation distance is not an optical distance physically involved in the setup, but is a function of the displacement of the sample with respect to both plane in focus.

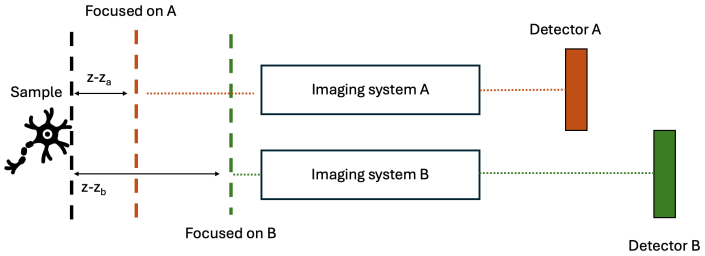

Fig. 1. Schematics of a generic CPI architecture

3.2. *Unapproximated evaluation of refocusing with a Gaussian object*

In order to appreciate what contributions to the final image quality are overlooked in the infinite-NA approximation, we now evaluate the complete refocused image in the simple scenario of a Gaussian object. In fact, the gaussian assumption on the sample allows us to deal with a completely analytical expression for refocusing. For definiteness, the analysis will be carried out for a microscopy-oriented CPI architecture, known as a correlation light-field microscope (CLM) [34,63]. The schematics of the optical design are illustrated in Fig. 2: light emitted by the sample propagates towards the entrance pupil of a microscope objective lens, after which it is

Optics EXPRESS

split into two optical arms; the arm leading to detector A is an M_a-magnification conventional microscope, arranged in such a way that the plane on focus on A is the first focal plane of the objective lens; on detector B, the second principal plane of the objective lens is imaged which, in a thin-lens approximation, can be considered as the objective lens plane. By choosing a reference coordinate system having the zero on the lens plane, one has, in the formalism of the previous section, $z_a = f$, where f is the objective focal length, and $z_b = z$ equal to the distance z of the object from the lens.

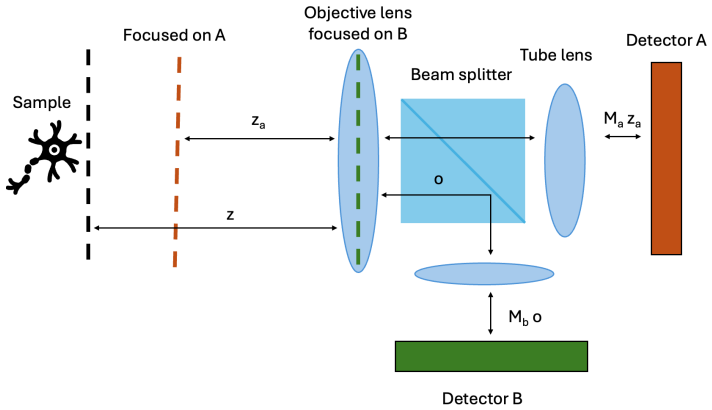

Fig. 2. Schematics of CLM

According to the approximated Eqs. (17) and (18), the predicted reconstructed image is the diffraction figure originating from the object, as observed from the equivalent distance

$$d_{\mathrm{CLM}}(z) = \left(\frac{1}{z-f} - \frac{1}{z}\right)^{-1}. \tag{19}$$

When the object is a Gaussian transmissive slit $|A(\boldsymbol{r_s})|^2 = \exp\left[-\frac{\boldsymbol{r_s^2}}{2\sigma_o^2}\right]$, Eq. (17) becomes

$$\Sigma_z^{(\infty)}(\boldsymbol{r}) = \exp\left[-\frac{\boldsymbol{r^2}}{2(\sigma_o^2/2 + \sigma(z)^2_{\mathrm{diff}})}\right] \qquad \text{with} \quad \sigma_{\mathrm{diff}}(z) = \frac{\lambda\, d_{\mathrm{CLM}}(z)}{2\sqrt{2}\pi\, \sigma_o}\ . \tag{20}$$

If the object is in focus ($f = z$, $\sigma_{\mathrm{diff}}(f) = 0$), Eq. (17) predicts that the reconstructed image has the same Gaussian shape of the sample, shrinked by a factor $1/\sqrt{2}$; this prediction is in accordance to the known fact that, if all image degradation mechanisms are neglected, a CPI image is the *squared* intensity profile of the object [51,53]. When $z \neq f$, instead, the predicted broadening is inversely proportional to the object size and directly proportional to the equivalent distance, as expected for the diffraction pattern from an aperture.

Let us now compare the prediction in the infinte-NA approximation with the expression of the real refocused image. By assuming the limiting aperture of the setup is determined by the objective lens acceptance, as is typically the case in conventional microscopy, both the tube lens and the lens imaging the objective onto detector B can be approximately assumed to be infinitely extended. For simplicity, we shall assume that the objective lens has Gaussian apodization, so that its PSF function is also Gaussian; the width of the lens will be assumed to be σ_l. To keep our analysis as general as possible, let us also include the possibility of a *misfocused* reconstruction: so far, we have only considered the case of perfect refocusing, namely, when the refocusing procedure reconstructs exactly the plane in which the object is. In most practical cases, however, the axial position of the sample is not known *a priori*, so that refocusing is performed on a whole

Optics EXPRESS

axial range, with the correct reconstruction being the sharpest image extracted from the whole z-scan. To account for possible misfocusing, let us consider the general form of refocusing at position z', possibly different from the true object position z. The resulting image reads

$$\Sigma_{z'}(\boldsymbol{r}) = \exp\left[-\frac{\boldsymbol{r}^2}{2\left((\sigma_o'(z,z'))^2/2 + \sigma_{\text{Ray}}^2(z') + \sigma_{\text{diff}}^2(z,z') + \sigma_{CoC}^2(z,z')\right)}\right], \tag{21}$$

where

$$\begin{aligned} \sigma_o'(z,z') &= \frac{z'}{z}\sigma_o \simeq \sigma_o & \sigma_{\text{Ray}}(z') &= \frac{\lambda}{4\pi\,\sigma_l/z'} \simeq \frac{\lambda}{4\pi\,\sigma_l/z} \\ \sigma_{\text{diff}}(z,z') &= \frac{d_{\text{CLM}}(z)+\frac{z-z'}{2}\left(\frac{z}{f}-1\right)}{\sqrt{\left(z/\sqrt{2}\sigma_l\right)^2+8\pi^2\,\sigma_o^2/\lambda^2}} \simeq \frac{\lambda\, d_{\text{CLM}}(z)}{2\sqrt{2}\pi\,\sigma_o} & \sigma_{CoC}(z,z') &= |z-z'|\,\frac{\sigma_l}{2z}. \end{aligned} \tag{22}$$

From Eq. (21) we see that, apart from the broadening stemming from misfocused refocusing σ_{CoC}, which had been neglected in the previous case, the only missing contribution to broadening is the Rayleigh-limited resolution σ_{Ray}, determined by the effective NA. A deeper physical understanding of the origin of the broadening mechanisms involved in Eq. (21) is obtained by considering the approximated version of the various contributions, appearing as the rightmost equalities in σ_o', σ_{Ray} and σ_{diff}.

- For $\sigma_o'(z,z')$, we see that in presence of misfocusing ($z' \neq z$), the native size of the sample can appear broadened ($z'<z$) or shrinked ($z'>z$); such effect, however, can hardly be noticed due to the concurrent broadening induced the term $\sigma_{CoC}(z,z')$, which is the dominating effect in case of misfocusing. As can be easily verified, the ratio between the two effects is of order $\sigma_l/2\sigma_o$ which, for the typical aperture and object size involved in microscopy, is dominated by several orders of magnitude by σ_{CoC}. Hence, even when considering modest misfocusing $|z-z'|$, σ_o' can be approximated by the real size of the object σ_o;
- Through an analogous reasoning, the numerical aperture σ_l/z' appearing in the denominator of $\sigma_{\text{Ray}}(z')$ can be replaced with the *effective* NA σ_l/z, defined by the distance of the sample from the acceptance pupil, which has a much more defined physical meaning. This term is, thus, the typical broadening due to the Airy disk in the focused plane;
- The third and last approximation, carried over the term σ_{diff}, is based on two arguments. Firstly, at the numerator, the second term depends on the product between the misfocusing and the relative distance from focus $(z-f)/f$. In a microscopy-oriented optical setup, both this quantities are usually very small, the former for the same argument as the previous approximations, the latter because the typical region of space that can be investigated in CLM with high resolution needs to be around the working distance of the microscope; the second term in the numerator can thus be neglected. The denominator is instead dominated by the second term, since the first term becomes non-neglibible only for an very small object size, which is only available for reconstruction very close to focus; in such conditions, however, broadening is dominated by the Rayleigh limit. Hence, σ_{diff} has its physical origin exactly in the diffraction explained in terms of the infinite-NA approximation;
- Lastly, the σ_{CoC} term is responsible for the axial sectioning capabilities of CPI, as defined by the circle of confusion (CoC). In fact, the term describes the typical CoC blurring of standard defocused microscopy and photography, with its radius being directly proportional to both the misfocusing and the effective NA [64].

In summary, the only effect that is neglected in the infinite-NA approximation, when refocusing the object plane ($z' = z$), is the conventional blurring to to the Airy disk.

Optics EXPRESS

4. Discussion

By analyzing Eq. (21), we have found that, in the case of a Gaussian object, the approximate form of the refocused image obtained by neglecting finite apertures (Eq. (17)) gives a rather good prediction of the image quality of a CPI reconstruction. In the absence of misfocusing, in fact, the broadening of the image due to diffraction is almost identical for the true refocus and approximated case. This is true, of course, provided the size of the imaged object is larger than the Rayleigh-limited resolution, where the broadening due to the NA-dependent Airy disk cannot be neglected. Such exception does not undermine the validity of our discussion: it is very well-known that CPI can reconstruct Rayleigh-limited object only around focus, while, in the rest of the 3D volume accessible for reconstruction, the imaging capabilities of the techniques are inherently limited to larger object size, as defined by the *resolution curves* [57]. To account for the Rayleigh limit at focus, the analytical expression of a CPI reconstruction can thus be summarized as

$$\Sigma_{z'=z}(\boldsymbol{r}) = \begin{cases} \left(\int |A(\boldsymbol{r}_s)|^2 \, |\mathcal{P}_0(\boldsymbol{r}_s - \boldsymbol{r})|^2 \, d\boldsymbol{r}_s \right)^2 & \text{when in focus} \\ \left| \int |A(\boldsymbol{r}_s)|^2 \exp\left[i \frac{\pi}{\lambda d(z)} (\boldsymbol{r}_s - \boldsymbol{r})^2 \right] d\boldsymbol{r}_s \right|^2 & \text{when out of focus} \end{cases}, \tag{23}$$

where $|\mathcal{P}_0|^2$ is the typical *incoherent* PSF of the imaging system in its focus. The optical performance of CPI can thus be attributed to two different physical phenomena, depending on the axial position of the object to reconstruct:

- Close to focus, image quality is determined by blurring, as is the case with typical imaging, determined by the convolution with a positive PSF (Airy disk), whose size is governed by the NA of the imaging system;
- Far from focus, image degradation is purely determined by *coherent* diffraction, by an equivalent free-space distance $d(z)$ that depends on the particular CPI architecture.

The imaging performance of CPI can thus be explained almost entirely in terms of Eq. (23), neglecting, for a moment, the axial sectioning capabilities. As it has been recently demonstrated, in fact, the image quality of a coherently illuminated defocused imaging system is not determined by CoC-induced blurring, as is the case with conventional imaging [65]. The resolution of coherent systems has been shown to be independent of NA and obey a square-root law with the distance from focus. In a complete analogy to coherent imaging, inspired by the striking similarity between Eq. (23) and the optical response of such systems, one can expect to derive the optical behavior of CPI entirely in terms of coherent imaging, with the caveat that the distance from focus, determining the resolution, must be replaced with the *equivalent* distance $d(z)$. To confirm that such analogy is indeed correct, let us remark that the resolution of defocused coherent systems can be explained purely in terms of diffraction from the object plane to the plane in focus [65], as described by square-root resolution loss with the distance from focus. Hence, the analogous resolution limit of CPI is expected to be

$$\mathrm{res}_{\mathrm{CPI}}(z) \propto \sqrt{\lambda \, d(z)}. \tag{24}$$

This expectation is, in fact, in perfect accordance with the all the well-known resolution curves of all the CPI architectures known to-date [33–35,54,55,57], demonstrating from yet another viewpoint that the analogy between CPI and coherent imaging is accurate. We must point out that, even if the arguments proposed so far have only been motivated analytically in the easy and unrealistic case of a Gaussian object, the validity of such arguments can be verified numerically for any other class of objects. For instance, Fig. 3 reports the results of a z'-scan, obtained by

Optics EXPRESS

refocusing a range of axial coordinates z' around the object position $z = 1000\,\mu$m. For brevity, we shall indicate with z or z' the displacement from focus (instead of $z - f$). The plots are obtained by assuming a CLM architecture (Fig. 2), where the Gaussian-apodized objective lens has focal length $f = 30$ mm, and NA$= \sigma_l/f = 0.167$. As the sample, a binary double-slit transmissive mask has been chosen, whose slits have center-to-center distance of 50 μm and width of 25 μm. On the left, the (x, z) section of the volumetric cube is reported, evaluated at fixed $y = 0$. From the plot, the axial sectioning capabilities of CPI are evident: when planes different from the true object plane are reconstructed ($z' \neq z$), the reconstruction appears blurred. As already mentioned when discussing Eq. (21), the origin of such blurring is the CoC, as defined by the NA, which is increasingly more severe as the misfocusing distance $|z - z'|$ increases. We should stress an important aspect of the CoC affecting CPI reconstructions, which is perfectly analogous to the propreties already demonstrated for 3D imaging through localized coherent illumination [65]: since a single coherent image (such as any 2D slice of the correlation function, as per Eq. (3)) does not suffer from CoC-induced blurring, the existence of a CoC enabling axial localization is a property of the refocusing algorithm, which yields a blurred image whenever the refocusing coordinate does not coincide with the sample coordinate ($z' \neq z$) [57]. Being a linear effect (*i.e.* a PSF), the CoC affects the reconstruction quality independently of the object characteristics; hence the NA-dependent axial sectioning of the refocusing procedure is the same regardless of the sample features, and is not a result of our choice of a Gaussian object profile in Eq. (21).

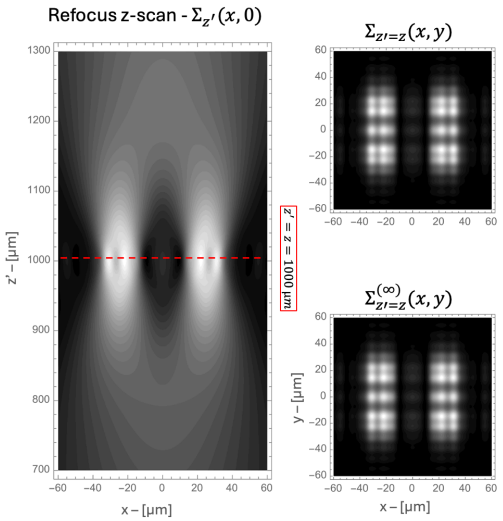

Fig. 3. Plots of the refocused images $\Sigma_{z'}(\boldsymbol{r})$ of a 50-μm double slit object placed at $z = 1000\,\mu$m. *Left:* software z-scan obtained by refocusing the axial range $700\,\mu\text{m} \leq z' \leq 1300\,\mu$m around the object. *Right:* comparison between the actual refocusing, without any approximation (top), and the image $\Sigma^{(\infty)}$, obtained by neglecting the finite size of pupils (top).

On the right-hand side of Fig. 3, the image extracted from the 3D reconstructed cube at perfect refocusing ($z' = z$) is reported (upper image). The image, obtained without performing any approximation on the correlation function and refocusing procedure, is indistinguishable from the image obtained by applying Eq. (17) directly to the object: for the object size in play, the pure diffraction (infinite-NA) approximation is an excellent framework for predicting the form of the final image, even for more conventional samples such as a double-slit mask. This equivalence between the CoC-free reconstruction in $z' = z$ and a diffraction pattern in a coherent imaging context allows us to give a pyisical explanation to the NA$\rightarrow \infty$ limit used to obtain our results: as

Optics EXPRESS

demonstrated both theoretically and experimentally [65], the most relevant contribution to image degradation in coherent systems derive from free-space diffraction from the object plane to the plane in focus. This is true, of course, provided the sample details to be imaged are larger than the Airy disk. By comparison with Eq. (12), we see that also in CPI the electric field impinging on the detectors is affected by diffraction by the defocusing distance $z_{a,b} - z$, and additionally blurred by the Airy disk. Therefore, the infinite-NA approximation in this context, entailing a point-like Airy disk in Eq. (12), is exactly the coherent-imaging analogous to considering diffraction to the planes at focus as the main source of image degradation.

When the object size is not large enough for the approximation infinite-NA to be accurate, but still the defocusing is sufficient to see some diffraction-induced fringing, the image shape cannot be described by any of the two cases presented in Eq. (23). This situation can be expected to be almost irrelevant in high-NA imaging system, where a very small natural DOF (λ/NA^2) implies a steep transition from the Rayleigh-limited (inside the natural DOF), to the diffraction-limited regimes. For systems with a modest NA, such as the one we are considering, the transition between the two cases can be smother, so that there might be a relevant region of 3D space that is not correctly described by either of the two regimes. Figure 4 shows the case of a 5 μm double slit, placed only 10 μm away from focus. The object size is barely larger than the Rayleigh-limited resolution, expected to be of about 3 μm, and the axial placement is slightly outside of the natural DOF. By comparing the image from unapproximated refocusing (top left) and the pure-diffraction image (top right), one immediately recognizes that, even with clear effects of the harmonic distortion caused by diffraction, non-negligible effect of blurring due to the Airy disk is still very evident in the first image. Blurring is evident by considering the plot in the middle, reporting the linear x-section at $y = 0$ of the two images above. The image obtained by coherent propagation (red line) shows much richer harmonic content than the actual image obtained through refocusing (blue line). By analyzing the harmonic content of the two curves (bottom panel), reported as the square module of the FFT on a logarithmic scale, the refocused image can be recognized as a low-pass filtered version of the coherent image. The attenuation of the high-frequency content can be explained by considering that blurring due to the Airy disk is indeed equivalent to a spatial frequency filter of width $2\,\mathrm{NA}/\lambda$ in the frequency domain (see Eq. (21)). To encompass this effect into a general-purpose formula, even if not perfectly accurate from the point of view of the derivation, Eq. (23) can be modified to account for the transient regime as

$$\Sigma_{z'=z}(\boldsymbol{r}) \simeq \int \left|\mathcal{P}_0\left(\boldsymbol{r}-\boldsymbol{r}'\right)\right|^2 \left| \int \left|A\left(\boldsymbol{r}_s\right)\right|^2 \exp\left[i \frac{\pi}{\lambda\, d(z)} \left(\boldsymbol{r}_s - \boldsymbol{r}'\right)^2 \right] d\boldsymbol{r}_s \right|^2 d\boldsymbol{r}', \tag{25}$$

which has the property of degenerating into the two limit cases when their respective conditions are satisfied, but to also include filtering due to the Airy disk in the intermediate scenario.

4.1. Validation with pseudo-thermal illumination

We shall now compare the predictions of our model to the real-life case in which the correlation function (Eq. (1)) is evaluated from a discrete and finite set of *speckle patterns* [66]. Experimental CPI datasets thus consist of two sets of N images $I^{(n)}_{A,B}(x_{a,b}, y_{a,b})$, as measured by the two detectors A and B, with $n = 1, \ldots, N$. The four-dimensional correlation function of Eq. (1) is thus estimated as the time average of the dataset

$$\Gamma_{\mathrm{exp}}(x_a, y_a, x_b, y_b) = \frac{1}{N}\sum_{n=1}^{N} I_A^{(n)} \otimes I_B^{(n)} - \left(\frac{1}{N}\sum_{n=1}^{N} I_A^{(n)}\right) \otimes \left(\frac{1}{N}\sum_{n=1}^{N} I_B^{(n)}\right). \tag{26}$$

Once the experimental correlation function is evaluated, the refocusing procedure described by Eq. (4) can be applied without any difference from the theoreical case. The number of meaured frames does not affect the optical performance of the techique (resolution and depth of field),

Optics EXPRESS

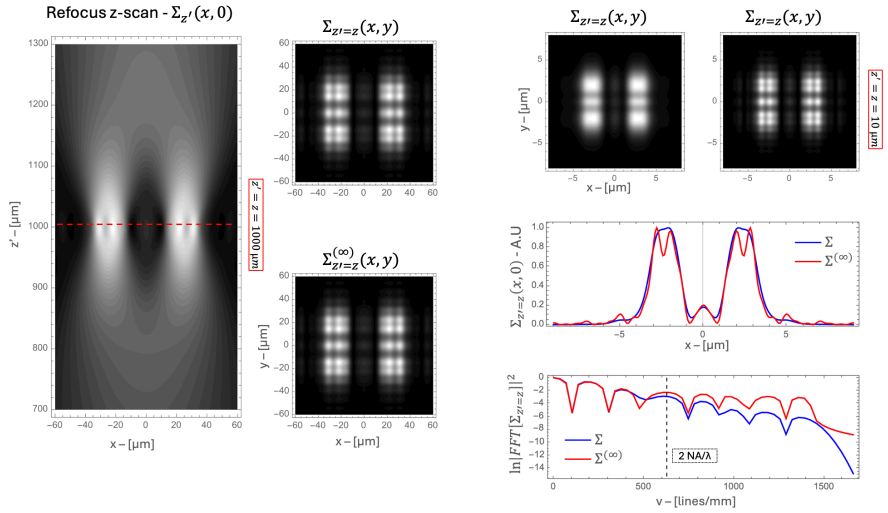

Fig. 4. Simulation showing the effect of neglecting finite apertures on small objects with slit separation of 5 μm and small displacement $z = 10\,\mu$m. *Top:* comparison between the unapproximated refocusing (left) and the infinite-NA case (right). *Middle;* 1D x- axis section of the refocused images, obtained by fixing the y coordinate; the plot compares the difference the unapproximated (blue) and infinite-NA (red) refocusing. *Bottom:* comparison of the fast Fourier transforms (FFT) of the data shown in the plot above. The dashed black vertical line reports the expected cutoff frequency on the unapproximated case, as determined by the Rayleigh limit, corresponding to an attenuation by a factor $1/e$.

whereas the SNR of the final images is heavily affected by N [58,59]. Our model, however, has been developed in the approximation of a infinite-SNR correlation function ($N \to \infty$), so that a fair comparison between Eq. (25) and the experimental refocusing can only be carried out if the latter is available with sufficiently high SNR.

Due to the requirement of a large number of frames, we choose to validate our model in one dimension, namely, on the x-components of the correlation function: the SNR of CPI is inversely proportional to the number of statistically independent modes of the electric field emitted by the object, resulting in a required N that is needlessly too large for our needs. In fact, provided the PSF $\mathcal{P}_{a,b}$ of the imaging systems (see Eq. (12)) is approximately factorized in the two dimensions

$$\mathcal{P}_{a,b}\left(\boldsymbol{r}_0, \frac{\boldsymbol{r}_{a,b}}{M_{a,b}}\right) \simeq \mathcal{P}^{(1D)}_{a,b}\left(x_0, \frac{x_{a,b}}{M_{a,b}}\right) \mathcal{P}^{(1D)}_{a,b}\left(y_0, \frac{y_{a,b}}{M_{a,b}}\right), \tag{27}$$

then also the refocused image is made up of indipendend contributions on the two dimensions

$$\Sigma_{z'}(\boldsymbol{r}) = \Sigma_{z'}(x)\,\Sigma_{z'}(y), \tag{28}$$

so that the model can be validated along only one dimension without any loss of generality.

Figure 5 shows a comparison between the theoretical model (Eq. (25)) and the refocused image obtained from a simulated CPI dataset, assuming the sample is an emitter of pseudo-thermal light. The experimental setup is the CLM architecture of Fig. 2, with an objective focal length $f = z_a = 30$ mm and an entrance pupil with 15 mm diameter, resulting in NA=0.25. In order to avoid undersampling, which might induce a pixel-limited optical performance, we have chosen a spatial sampling about three times smaller than the Airy disk size λ/NA. The sample is a 50 μm center-to-center double slit, placed out of focus by a distance $z - z_a = 1$ mm. The reconstructed image prescribed by the model (solid blue line) has been obtained by propagating the sample

Optics EXPRESS

profile by an equivalent distance $d_{\mathrm{CLM}}(z)$ (Eq. (19)) through Fourier optics, and then by blurring with the Raylrigh-limited PSF of the sytesm $|\mathcal{P}_A|^2$. The dashed gray and solid red lines report, respectively, a low-SNR and high-SNR refocusing. The low-SNR measurement is obtained by evaluating the correlation function from $N = 10^3$ frames, whereas the high-SNR is obtained from $N = 10^5$. Simulated datasets are obtained by generating N speckle patterns with random phase and exponentially decreasing intensity distribution, as expected for a pseudo-thermal emission; each speckle pattern is multiplied by the object double-slit emission profile, resulting in point-like correlated emission on the sample area; spatial (detector A) and angular (detector B) frames are obtained by propagating each speckle pattern through the optical setup by using Fourier optics; intensity distributions are obtained as the square module of each of the $2N$ speckle patterns; the correlation function is then evaluated by applying Eq. (26) and refocused.

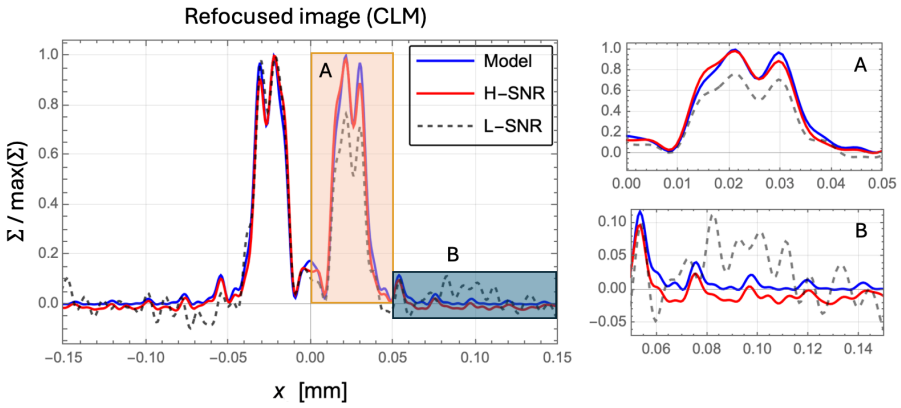

Fig. 5. Validation of the model on simulated speckle-patterns in the CLM setup of Fig. 2. The sample is a 50 μm center-to-center double slit. The solid blue line is the theoretical expectation, as prescribed by Eq. (25); the dashed gray line is obtained by refocusing a low-SNR correlation function ($N = 10^3$), whereas the red line is the refocusing of a high-SNR correlation function ($N = 10^5$). The A and B insets show, respectively, the details corresponding to the refocused slit area and background.

As can be seen from the figure, the theoretical prediction is extremely similar to the refocused image obtained be refocusing the correlation function obtained, in turn, from pixel-by-pixel correlation of speckle patterns. In fact, the two images evaulate to a Pearson correlation coefficient of 99.6%.

Figure 6 reports the comparison between the theoretical expectation and simulated speckled dataset in another CPI architecture, named CPI-AP [54]. The simulated experimental setup is shown in panel a): detectors A and B are arranged in such a way that the imaged planes are imaged planes are placed at $z_a = f - 0.5$ mm and $z_b = f + 0.5$ mm, respectively. Each of the two optical paths is thus a two-lens microscope-like design, neither focused at the working distance ($z_{a,b} \neq f$). As for the simulations in Fig. 5, the focal length of the first lens is $f = 30$ mm, with a diameter of 15 mm. The sample, chosen as a double slit with the same size as Fig. 5 is placed mid-way between z_a and z_b, namely, $z = f \neq z_{a,b}$. Both the theoretical curve and the simulation of the speckled dataset is obtained as in the previous case. Due to an evidently lower SNR compared to the previous case, a comparison between the refocused correlation function from experimental data and the theoretical model results in a 65.7% correlation coefficient.

Regardless of the absolute value of the correlation coefficient, which is heavily dependent on the SNR of the reconstruction and how well the approximated expression of Eq. (25) reproduces experimental reality, Figs. 5 and 6 show that the experimental fringing effects experimentally found in CPI can be perfectly explained as diffraction fringes. In fact, the axial position of peaks

Optics EXPRESS

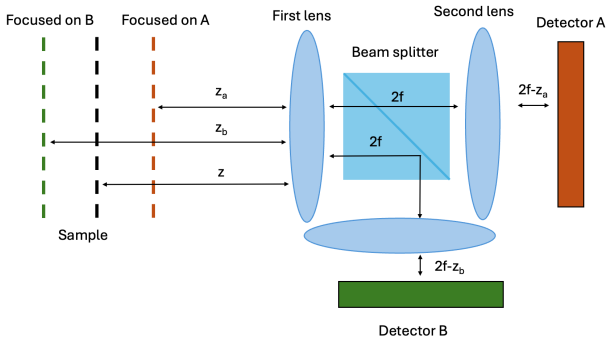

(a)

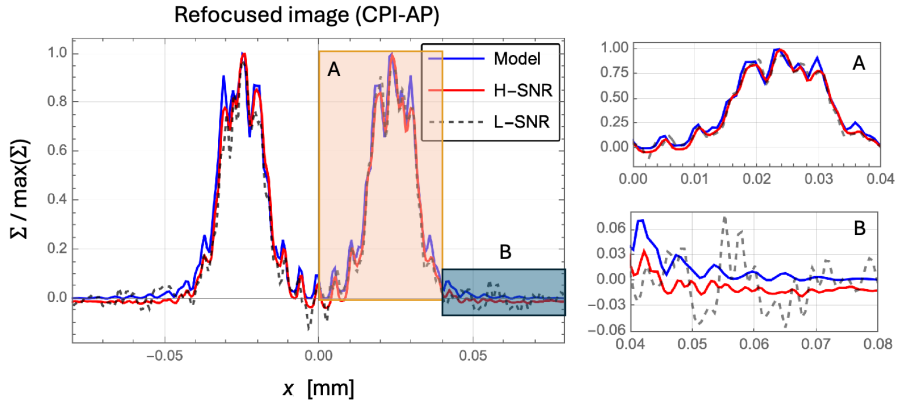

(b)

Fig. 6. Validation of the model on simulated speckle-patterns in a CPI-AP setup [54]. The sample is the same double slit mask as in Fig. 5. *Panel a).* Experimental scheme of the simulated CPI-AP architecture. *Panel b).* The solid blue line is the theoretical expectation; the dashed gray line is obtained by refocusing a low-SNR correlation function ($N = 10^3$); red line is the refocusing of a high-SNR correlation function ($N = 10^5$). The A and B insets show, respectively, the details corresponding to the refocused slit area and background.

and dips of the refocused images is accurately predicted, both for CLM and CPI-AP, by the theoretical model we developed.

5. Conclusions

Neglecting the finite size of the apertures in the optical design of CPI has allowed us obtain the mathematical expression relating the shape of the object to the final image obtained through CPI refocusing. The motivation for investigating such infinite-NA approximation is well-rooted in previous literature, containing abundant experimental and theoretical evidence that the quality of refocused images is mostly independent of the size of the optics. As recently demonstrated, the NA indeed plays a key role in determining the tomographic capabilities of CPI [57], but the lateral resolution is determined by a square-root trend depending the optical distances involved, with no contribution from the NA.

The analytical expression of the refocused images (Eq. (23)) has allowed us to bridge the gap between the phenomenological characterization of the imaging performance of the technique,

Optics EXPRESS

extensively demonstrated in previous literature, and the explanation of the physical origin of that performance. In fact, Eq. (23) implies that a defocused CPI system performs exactly as an optical system illuminated by a spatially coherent source of light [65]. The resolution in such systems has, in fact, the very same features already known for CPI, such as the square-root dependence of the resolution on the distance from focus. Two differences, however, must be highlighted: firstly, the propagation distance in the case of CPI must be substituted with an *equivalent* distance $d(z)$, which only degenerates into a pure square-root law only in the case of CPI through position-momentum correlations ($z_b \to \infty$ in Eq. (18)) [55]; lastly, whereas coherent imaging is sensitive to the phase content of the sample, CPI in the case of $m = 1$ (see Eq. (3)) is phase-insensitive. Architectures where the object is placed only in one of the two optical arms, however, can be expected to gain the same phase sensitivity as coherent imaging, although with a reduced SNR [58,59].

To conclude, we should point out that the availability of an analytical form of the output image can be expected to greatly improve the volumetric imaging capabilities of CPI. In fact, the optical performance of the technique has been so far evaluated by studying how faithfully an object can be reconstructed as a function of its axial position. The *resolution curves* of the technique where thus obtained by selecting, for each axial position, the smallest object size resulting in a satisfactory reconstruction. However, as we show in Fig. 7, even with very large displacement from focus, images reconstructed by CPI (blue) are never "washed away", as is the case with conventional incoherent imaging systems, but show rich spatial modulation. Such spatial features, which in past literature were considered as artifacts of the technique, can now be deterministically related to the object shape through Eq. (23). Hence, even with axial displacements so large that the final image does not resemble the original shape of the sample, the object can be recovered by means of broadly-used inverse computation algorithms, used on a daily basis in conventional coherent imaging techniques, paving the way towards even better reconstruction capabilities and super-resolution [67–69].

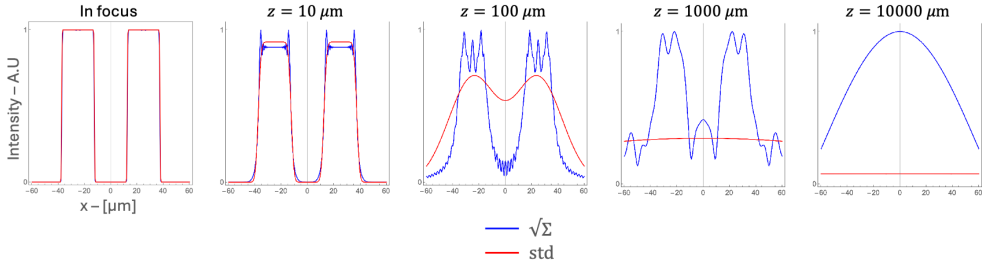

Fig. 7. Comparison of the different type of image degradation affecting CPI refocused images (blue) and standard incoherent imaging (red), as the object is moved away from focus ($z = 0$). The object is a 50 μ double slit object, as in Fig. 3.

Funding. European Defence Fund (EDF-2021-DIS-RDIS-ADEQUADE (n° 101103417)).

Acknowledgments. This article has benefited from the contributions of prof. M. D'Angelo, who obtained project funding.

Disclosures. The author declares no conflicts of interest.

Data availability. Data underlying the results presented in this paper may be obtained upon request to the author.

References

1. V. Giovannetti, S. Lloyd, and L. Maccone, "Advances in quantum metrology," Nat. Photonics **5**(4), 222–229 (2011).
2. A. Zavatta, M. D'Angelo, V. Parigi, *et al.*, "Remote preparation of arbitrary time-encoded single-photon ebits," Phys. Rev. Lett. **96**(2), 020502 (2006).
3. T. Iskhakov, A. Allevi, D. Kalashnikov, *et al.*, "Intensity correlations of thermal light: noise reduction measurements and new ghost imaging protocols," Eur. Phys. J. Spec. Top. **199**(1), 127–138 (2011).

Optics EXPRESS

4. A. Avella, I. Ruo-Berchera, I. P. Degiovanni, *et al.*, "Absolute calibration of an emccd camera by quantum correlation, linking photon counting to the analog regime," Opt. Lett. **41**(8), 1841–1844 (2016).
5. A. Agliati, M. Bondani, A. Andreoni, *et al.*, "Quantum and classical correlations of intense beams of light investigated via joint photodetection," J. Opt. B: Quantum Semiclassical Opt. **7**(12), S652–S663 (2005).
6. A. Allevi, S. Olivares, and M. Bondani, "Measuring high-order photon-number correlations in experiments with multimode pulsed quantum states," Phys. Rev. A **85**(6), 063835 (2012).
7. T. B. Pittman, Y.-H. Shih, D. V. Strekalov, *et al.*, "Optical imaging by means of two-photon quantum entanglement," Phys. Rev. A **52**(5), R3429–R3432 (1995).
8. T. Pittman, D. Strekalov, D. Klyshko, *et al.*, "Two-photon geometric optics," Phys. Rev. A **53**(4), 2804–2815 (1996).
9. I. N. Agafonov, M. V. Chekhova, T. S. Iskhakov, *et al.*, "High-visibility intensity interference and ghost imaging with pseudo-thermal light," J. Mod. Opt. **56**(2-3), 422–431 (2009).
10. R. S. Aspden, D. S. Tasca, R. W. Boyd, *et al.*, "EPR-based ghost imaging using a single-photon-sensitive camera," New J. Phys. **15**(7), 073032 (2013).
11. M. Cassano, M. D'Angelo, A. Garuccio, *et al.*, "Spatial interference between pairs of disjoint optical paths with a single chaotic source," Opt. Express **25**(6), 6589–6603 (2017).
12. Y. Bai and S. Han, "Ghost imaging with thermal light by third-order correlation," Phys. Rev. A **76**(4), 043828 (2007).
13. M. Bina, D. Magatti, M. Molteni, *et al.*, "Backscattering differential ghost imaging in turbid media," Phys. Rev. Lett. **110**(8), 083901 (2013).
14. G. Brida, M. Chekhova, G. Fornaro, *et al.*, "Systematic analysis of signal-to-noise ratio in bipartite ghost imaging with classical and quantum light," Phys. Rev. A **83**(6), 063807 (2011).
15. Y. Bromberg, O. Katz, and Y. Silberberg, "Ghost imaging with a single detector," Phys. Rev. A **79**(5), 053840 (2009).
16. K. W. C. Chan, M. N. O'Sullivan, and R. W. Boyd, "Two-color ghost imaging," Phys. Rev. A **79**(3), 033808 (2009).
17. M. D'Angelo, A. Valencia, M. H. Rubin, *et al.*, "Resolution of quantum and classical ghost imaging," Phys. Rev. A **72**(1), 013810 (2005).
18. B. I. Erkmen and J. H. Shapiro, "Ghost imaging: from quantum to classical to computational," Adv. Opt. Photonics **2**(4), 405–450 (2010).
19. F. Ferri, D. Magatti, A. Gatti, *et al.*, "High-resolution ghost image and ghost diffraction experiments with thermal light," Phys. Rev. Lett. **94**(18), 183602 (2005).
20. M. D'Angelo, A. Mazzilli, F. Pepe, *et al.*, "Characterization of two distant double-slits by chaotic light secondorder interference," Sci. Rep. **7**(1), 2247 (2017).
21. F. Ferri, D. Magatti, L. Lugiato, *et al.*, "Differential ghost imaging," Phys. Rev. Lett. **104**(25), 253603 (2010).
22. Y. Shih, "The physics of turbulence-free ghost imaging," Technologies **4**(4), 39 (2016).
23. Z.-H. Xu, W. Chen, J. Penuelas, *et al.*, "1000 fps computational ghost imaging using led-based structured illumination," Opt. Express **26**(3), 2427–2434 (2018).
24. A. Paniate, G. Massaro, A. Avella, *et al.*, "Light-field ghost imaging," Phys. Rev. Appl. **21**(2), 024032 (2024).
25. P.-A. Moreau, E. Toninelli, T. Gregory, *et al.*, "Imaging with quantum states of light," Nat. Rev. Phys. **1**(6), 367–380 (2019).
26. G. Brida, M. Genovese, and I. Ruo-Berchera, "Experimental realization of sub-shot-noise quantum imaging," Nat. Photonics **4**(4), 227–230 (2010).
27. N. Samantaray, I. Ruo-Berchera, A. Meda, *et al.*, "Realization of the first sub-shot-noise wide field microscope," Light: Sci. Appl. **6**(7), e17005 (2017).
28. G. Ortolano, A. Paniate, P. Boucher, *et al.*, "Quantum enhanced non-interferometric quantitative phase imaging," Light: Sci. Appl. **12**(1), 171 (2023).
29. A. Allevi, S. Cassina, and M. Bondani, "Super-thermal light for imaging applications," Quantum Measurements and Quantum Metrology **4**(1), 26–34 (2017).
30. A. Gatti, E. Brambilla, M. Bache, *et al.*, "Ghost imaging with thermal light: comparing entanglement and classical correlation," Phys. Rev. Lett. **93**(9), 093602 (2004).
31. M. N. O'Sullivan, K. W. C. Chan, and R. W. Boyd, "Comparison of the signal-to-noise characteristics of quantum versus thermal ghost imaging," Phys. Rev. A **82**(5), 053803 (2010).
32. A. Valencia, G. Scarcelli, M. D'Angelo, *et al.*, "Two-photon imaging with thermal light," Phys. Rev. Lett. **94**(6), 063601 (2005).
33. M. D'Angelo, F. V. Pepe, A. Garuccio, *et al.*, "Correlation plenoptic imaging," Phys. Rev. Lett. **116**(22), 223602 (2016).
34. G. Massaro, D. Giannella, A. Scagliola, *et al.*, "Light-field microscopy with correlated beams for high-resolution volumetric imaging," Sci. Rep. **12**(1), 16823 (2022).
35. G. Massaro, P. Mos, S. Vasiukov, *et al.*, "Correlated-photon imaging at 10 volumetric images per second," Sci. Rep. **13**(1), 12813 (2023).
36. C. Abbattista, L. Amoruso, S. Burri, *et al.*, "Towards quantum 3d imaging devices," Appl. Sci. **11**(14), 6414 (2021).
37. F. Scattarella, D. Diacono, A. Monaco, *et al.*, "Deep learning approach for denoising low-snr correlation plenoptic images," Sci. Rep. **13**(1), 19645 (2023).
38. I. Petrelli, F. Santoro, G. Massaro, *et al.*, "Compressive sensing-based correlation plenoptic imaging," Front. Phys. **11**, 1287740 (2023).

Optics EXPRESS

39. F. V. Pepe, F. Di Lena, A. Mazzilli, *et al.*, "Diffraction-limited plenoptic imaging with correlated light," Phys. Rev. Lett. **119**(24), 243602 (2017).
40. E. Adelson and J. Wang, M. I. of Technology. Media Laboratory. Vision, and M. Group, *Single Lens Stereo with a Plenoptic Camera*, M.I.T. Media Lab Vision and Modeling Group technical report (Vision and Modeling Group, Media Laboratory, Massachusetts Institute of Technology, 1992).
41. J. Pawley, *Handbook of biological confocal microscopy*, vol. 236 (Springer Science & Business Media, 2006).
42. I. Ihrke, J. Restrepo, and L. Mignard-Debise, "Principles of light field imaging: Briefly revisiting 25 years of research," IEEE Signal Process. Mag. **33**(5), 59–69 (2016).
43. R. Ng, M. Levoy, M. Brédif, *et al.*, "Light field photography with a hand-held plenoptic camera," Computer Science Technical Report CSTR **2**, 1–11 (2005).
44. R. Ng, "Fourier slice photography," ACM Trans. Graph. **24**(3), 735–744 (2005).
45. C. Birklbauer and O. Bimber, "Panorama light-field imaging," in *Computer Graphics Forum*, vol. 33-2 (Wiley Online Library, 2014), pp. 43–52.
46. M. Broxton, L. Grosenick, S. Yang, *et al.*, "Wave optics theory and 3-D deconvolution for the light field microscope," Opt. Express **21**(21), 25418–25439 (2013).
47. R. Prevedel, Y.-G. Yoon, M. Hoffmann, *et al.*, "Simultaneous whole-animal 3d imaging of neuronal activity using light-field microscopy," Nat. Methods **11**(7), 727–730 (2014).
48. T. Georgeiv, K. C. Zheng, B. Curless, *et al.*, "Spatio-angular resolution tradeoffs in integral photography," in *Proceedings of the 17th Eurographics Conference on Rendering Techniques*, (Eurographics Association, Goslar, DEU, 2006), EGSR '06, pp. 263–272.
49. B. Goldlücke, O. Klehm, S. Wanner, *et al.*, "Plenoptic cameras," *Digital Representations of the Real World: How to Capture, Model, and Render Visual Reality*, M. Magnor, O. Grau, O. Sorkine-Hornung, *et al.*, eds. (CRC Press, 2015) (2015).
50. G. Massaro, F. V. Pepe, and M. D'Angelo, "Refocusing Algorithm for Correlation Plenoptic Imaging," Sensors **22**(17), 6665 (2022).
51. G. Massaro, F. Di Lena, M. D'Angelo, *et al.*, "Effect of finite-sized optical components and pixels on light-field imaging through correlated light," Sensors **22**(7), 2778 (2022).
52. F. V. Pepe, F. Di Lena, A. Garuccio, *et al.*, "Correlation plenoptic imaging with entangled photons," Technologies **4**(2), 17 (2016).
53. F. Di Lena, F. Pepe, A. Garuccio, *et al.*, "Correlation plenoptic imaging: An overview," Appl. Sci. **8**(10), 1958 (2018).
54. F. Di Lena, G. Massaro, A. Lupo, *et al.*, "Correlation plenoptic imaging between arbitrary planes," Opt. Express **28**(24), 35857–35868 (2020).
55. D. Giannella, G. Massaro, B. Stoklasa, *et al.*, "Light-field imaging from position-momentum correlations," Phys. Lett. A **494**, 129298 (2024).
56. F. Scattarella, G. Massaro, B. Stoklasa, *et al.*, "Periodic patterns for resolution limit characterization of correlation plenoptic imaging," The European Physical Journal Plus **138**(8), 710 (2023).
57. G. Massaro, "Assessing the 3d resolution of refocused correlation plenoptic images using a general-purpose image quality estimator," (2024).
58. G. Massaro, G. Scala, M. D'Angelo, *et al.*, "Comparative analysis of signal-to-noise ratio in correlation plenoptic imaging architectures," The European Physical Journal Plus **137**(10), 1123 (2022).
59. G. Scala, M. D'Angelo, A. Garuccio, *et al.*, "Signal-to-noise properties of correlation plenoptic imaging with chaotic light," Phys. Rev. A **99**(5), 053808 (2019).
60. J. W. Goodman, *Introduction to Fourier optics* (Roberts and Company Publishers, 2005).
61. M. Levoy, R. Ng, A. Adams, *et al.*, "Light field microscopy," in *ACM SIGGRAPH 2006 Papers*, (Association for Computing Machinery, New York, NY, USA, 2006), SIGGRAPH '06, pp. 924–934.
62. B. E. Saleh and M. C. Teich, *Fundamentals of photonics* (Wiley Series in Pure and Applied Optics, Wiley, 2007).
63. A. Scagliola, F. Di Lena, A. Garuccio, *et al.*, "Correlation plenoptic imaging for microscopy applications," Phys. Lett. A **384**(19), 126472 (2020).
64. P. A. Stokseth, "Properties of a defocused optical system*," J. Opt. Soc. Am. **59**(10), 1314–1321 (1969).
65. G. Massaro, B. Barile, G. Scarcelli, *et al.*, "Direct 3d imaging through spatial coherence of light," Laser Photonics Reviews p. 2301155 (1992).
66. J. Goodman, *Speckle Phenomena in Optics: Theory and Applications* (Roberts & Company, 2007).
67. G. Zheng, C. Shen, S. Jiang, *et al.*, "Concept, implementations and applications of fourier ptychography," Nat. Rev. Phys. **3**(3), 207–223 (2021).
68. J. Marrison, L. Räty, P. Marriott, *et al.*, "Ptychography–a label free, high-contrast imaging technique for live cells using quantitative phase information," Sci. Rep. **3**(1), 2369 (2013).
69. L. Tian and L. Waller, "3d intensity and phase imaging from light field measurements in an led array microscope," Optica **2**(2), 104–111 (2015).